AGU PUBLICATIONS

Geochemistry, Geophysics, Geosystems

RESEARCH ARTICLE
10.1002/2017GC007097

Key Points:
- We investigate and upscale the physical and transport properties of an exceptionally exposed carbonate-bearing normal fault in central Italy
- Physical and transport properties of the investigated fault zone are controlled by the protolith and the different deformation processes
- Laboratory physical and mechanical data are in good agreement with in situ measurements and well-match seismological data

Correspondence to:
F. Trippetta,
fabio.trippetta@uniroma1.it

Citation:
Trippetta, F., Carpenter, B. M., Mollo, S., Scuderi, M. M., Scarlato, P., & Collettini, C. (2017). Physical and transport property variations within carbonate-bearing fault zones: Insights from the Monte Maggio Fault (central Italy). *Geochemistry, Geophysics, Geosystems*, *18*. https://doi.org/10.1002/2017GC007097

Received 29 JUN 2017
Accepted 16 OCT 2017
Accepted article online 20 OCT 2017

Physical and Transport Property Variations Within Carbonate-Bearing Fault Zones: Insights From the Monte Maggio Fault (Central Italy)

F. Trippetta[1], B. M. Carpenter[2], S. Mollo[1,3], M. M. Scuderi[1], P. Scarlato[3], and C. Collettini[1,3]

[1]Dipartimento di Scienze della Terra (DST), Sapienza Università di Roma, Roma, Italy, [2]School of Geology and Geophysics, University of Oklahoma, Norman, OK, USA, [3]Istituto Nazionale di Geofisica e Vulcanologia, Roma, Italy

Abstract The physical characterization of carbonate-bearing normal faults is fundamental for resource development and seismic hazard. Here we report laboratory measurements of density, porosity, V_p, V_s, elastic moduli, and permeability for a range of effective confining pressures (0.1–100 MPa), conducted on samples representing different structural domains of a carbonate-bearing fault. We find a reduction in porosity from the fault breccia (11.7% total and 6.2% connected) to the main fault plane (9% total and 3.5% connected), with both domains showing higher porosity compared to the protolith (6.8% total and 1.1% connected). With increasing confining pressure, *P* wave velocity evolves from 4.5 to 5.9 km/s in the fault breccia, is constant at 5.9 km/s approaching the fault plane and is low (4.9 km/s) in clay-rich fault domains. We find that while the fault breccia shows pressure sensitive behavior (a reduction in permeability from 2×10^{-16} to 2×10^{-17} m^2), the cemented cataclasite close to the fault plane is characterized by pressure-independent behavior (permeability 4×10^{-17} m^2). Our results indicate that the deformation processes occurring within the different fault structural domains influence the physical and transport properties of the fault zone. In situ V_p profiles match well the laboratory measurements demonstrating that laboratory data are valuable for implications at larger scale. Combining the experimental values of elastic moduli and frictional properties it results that at shallow crustal levels, $M \leq 1$ earthquakes are less favored, in agreement with earthquake-depth distribution during the L'Aquila 2009 seismic sequence that occurred on carbonates.

1. Introduction

Fault rocks and related properties such as permeability, frictional behavior, fluid content, and lithology exert a significant control on fault structure (Cowie & Scholz, 1992; Faulkner et al., 2010; and others), earthquake rupture nucleation, propagation and arrest (Ben-Zion & Sammis, 2003; Boatwright & Cocco, 1996), fluid flow (Caine, 1996; Evans et al., 1997; Mitchell & Faulkner, 2012), and variations in the stress field around brittle crustal faults (Faulkner et al., 2006). Fault structure is generally represented by one or more high strain slip zones (the fault core) surrounded by a highly heterogeneous region characterized by fracture sets, secondary faults, joints, and veins (damage zone). The intensity of deformation in the damage zone decays away from the fault into relatively undeformed host rocks (Caine, 1996; Chester & Logan, 1986; Faulkner et al., 2010; Savage & Brodsky, 2011). The described fault zone architecture has mainly been reconstructed from field examples of faults cutting across crystalline basement rocks (e.g., Chester & Logan, 1986; Mitchell & Faulkner, 2009). However, within fault zones crosscutting sedimentary rocks, the mechanical properties are significantly influenced by sedimentary facies, with different mineralogical characteristics that primarily affect grain size, grain distribution, and porosity (Hugman & Friedman, 1979; Riley et al., 2010; Shipton et al., 2006). Nonetheless, at first approximation, the typical fault zone structure where slip localizes along a fault core with distributed deformation in the damage zone, has also been documented also for carbonate-bearing faults (e.g., Agosta & Kirschner, 2003; Billi et al., 2003; Collettini et al., 2014a; Demurtas et al., 2016; Ferrill et al., 2011; Fondriest et al., 2012; Micarelli et al., 2006) with some notable differences highlighted in the width and in the mechanical processes acting on the damage zones (De Paola et al., 2008; Ferrill et al., 2011; Micarelli et al., 2006).

Carbonate-bearing faults represent important structures for numerous reasons, including: (1) faulted and fractured carbonate reservoirs contain approximately two thirds of the world's oil and gas reserves (Al-Anzi

et al., 2003), and (2) significant earthquakes, both natural (i.e., Miller et al., 2004) or human-induced (i.e., Improta et al., 2015) nucleate and/or propagate through thick sequences of carbonates that dominate upper-crustal sedimentary sequences (Burchfiel et al., 2008; Chiaraluce, 2012; Govoni et al., 2014; Nissen et al., 2014; Mirabella et al., 2008). For these reasons, the characterization of carbonate-bearing faults is fundamental to improve our understanding of reservoir characterization and seismic risk in active tectonic areas. In particular, the transport and mechanical properties of carbonate-bearing faults at crustal conditions have received increased attention (e.g., Agosta, 2008; Baud et al., 2009; Bussolotto et al., 2015; Michie, 2015; Michie & Haines, 2016; Rath et al., 2011) together with the characterization of the frictional properties (e.g., Carpenter et al., 2014, 2016; De Paola et al., 2015; Scuderi et al., 2016; Smith et al., 2013; Tesei et al., 2014; Violay et al., 2013; Verberne et al., 2010, 2014, 2015).

In this work, we investigate the physical properties of carbonate samples collected along the Monte Maggio Normal Fault (MMNF), a regional-scale normal fault zone located in the active extensional system of the Northern Apennines (Italy). We developed laboratory experiments to characterize the petrophysical properties of the different domains identified across the fault zone. Results are discussed to (1) infer the evolution of the fault physical properties during deformation; (2) compare laboratory determinations of V_p with field measurements; and (3) provide further constraints for earthquake nucleation on carbonate-bearing faults.

2. Field Study Area—The Monte Maggio Normal Fault

The study area (Figure 1) is located within the Northern Apennines (Italy), a thrust-and-fold belt resulting from the convergence between the Alpine orogen and the continental lithosphere of the African plate (e.g., Doglioni et al., 1998, and references therein). While convergence is still active beneath the Po River plain and along the Adriatic coast (Anderlini et al., 2016; Frepoli & Amato, 1997), extensional tectonics have

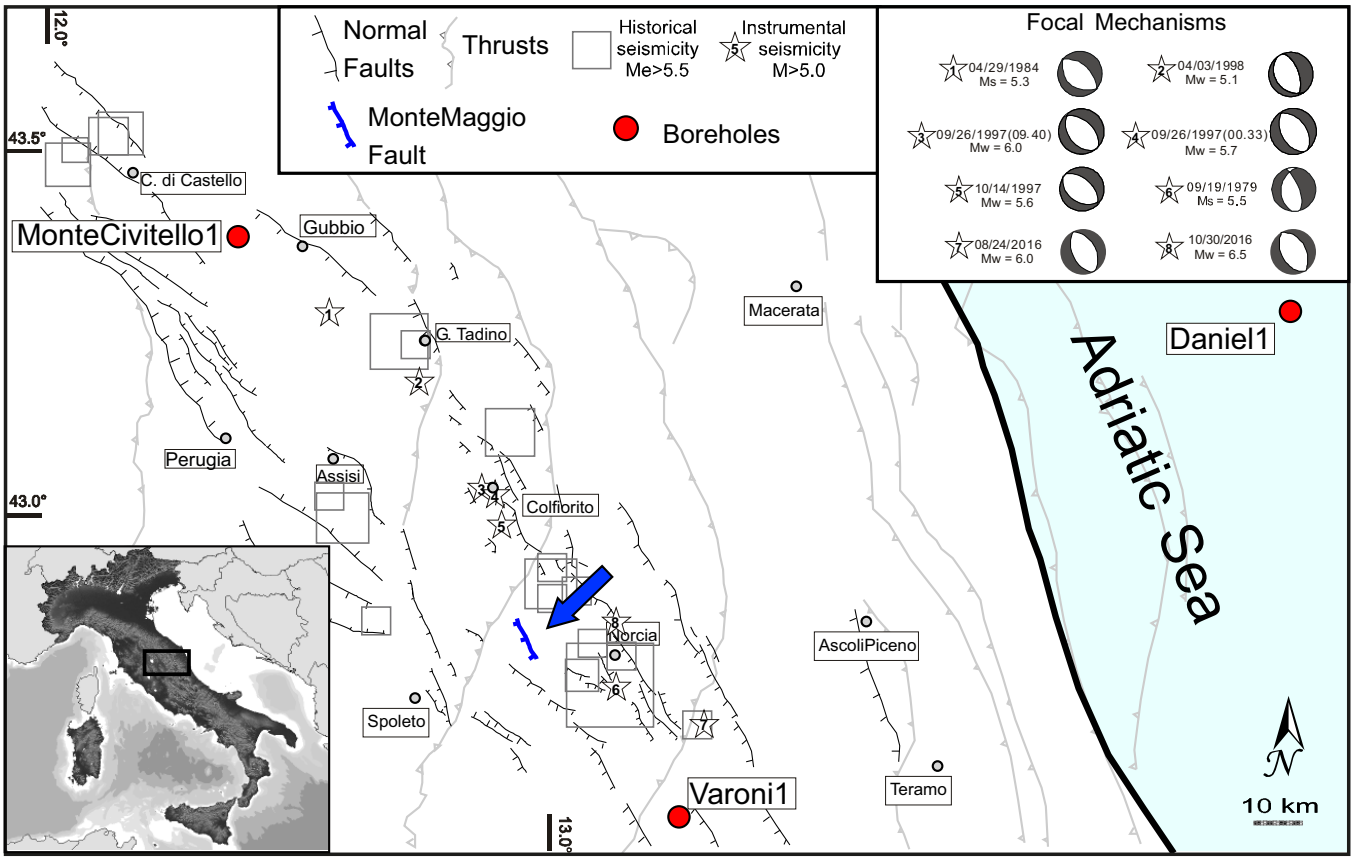

Figure 1. Simplified map of the Umbria–Marche Apennines of central Italy, with locations of the Monte Maggio Fault and of the boreholes analyzed for the comparison of measured V_p in Laboratory (modified after Lavecchia et al., 1994; Collettini et al., 2014b).

characterized the axial zone of the Northern Apennines since the upper Pliocene (Barchi et al., 1998; Collettini et al., 2006). The resulting extension is mainly accommodated by high-angle W-dipping normal faults, which are responsible for the major earthquakes of the area (e.g., Boncio & Lavecchia, 2000; Chiarabba et al., 2009; Chiaraluce et al., 2005, 2017; Collettini et al., 2003).

The Monte Maggio Normal Fault (MMNF) is a spectacularly exposed (Figure 2a), high-angle W-dipping normal fault outcropping near the town of Spoleto (central Italy). The MMNF is located in an area where regional uplift and erosion override sedimentation, therefore Quaternary basin filling sediments in the hanging-wall are absent. Slip on the fault results in the juxtaposition of carbonate formations of the Umbria-Marche sequence. We thus interpret the MMNF as an exhumed analogue of the active structures that, in the same area, are responsible for the recorded seismicity like the 1997 Colfiorito (Mw = 6.0), the 2009 (Mw = 6.3) L'Aquila and the 2016 Amatrice (Mw = 6.0) and Norcia (Mw = 6.5) earthquakes (Amato et al., 1998; Chiarabba et al., 2009; Chiaraluce et al., 2005, 2017; Mirabella et al., 2008; Tinti et al., 2016). The fault extends for a length of 10 km consisting of five subparallel segments with a maximum distance between overlapping fault segments of about 1.5 km. The maximum displacement (370–650 m) of each fault segment is partitioned along subparallel slipping zones extending for a total width of about 50 m (Collettini et al., 2014a). These slipping zones, developed within the calcare massiccio formation, are characterized by a prominent slip surface with different slip surface phenomena, including pluck-holes, grooves,

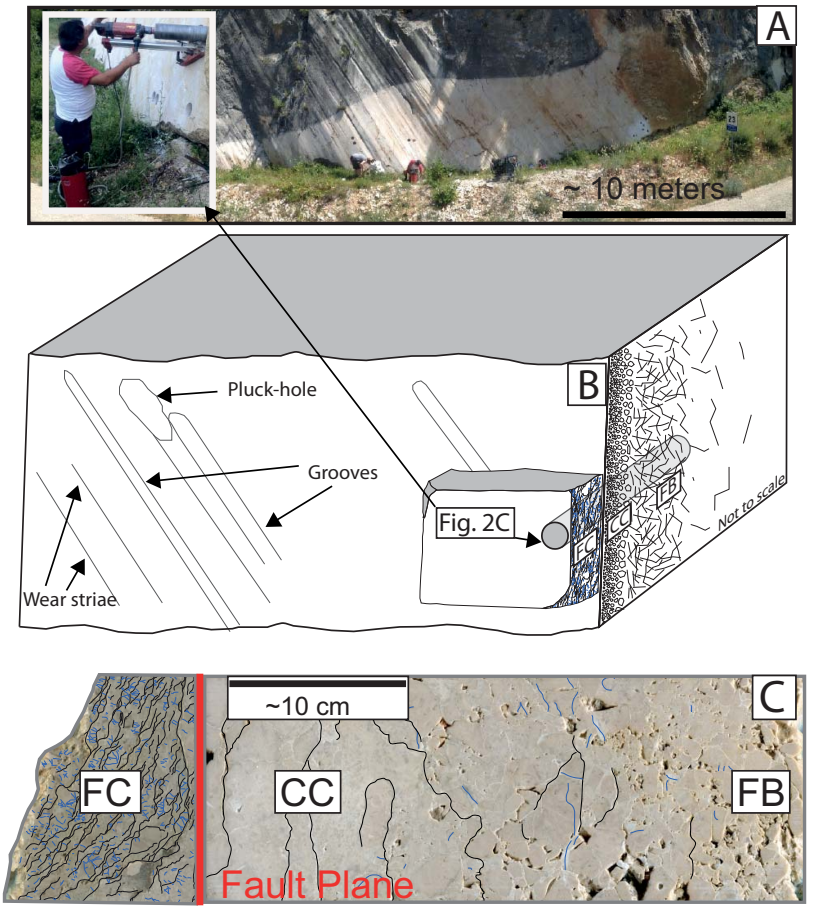

Figure 2. (a) Outcrop picture of the Monte Maggio Normal Fault and coring method (top left inset). (b) Schematic illustration of fault architecture. The slip surface shows grooves and striations at different scales. Fault plane juxtaposes a foliated cataclasite and a very thin ultracataclasite rock where this latter results from the comminution of a thicker cemented cataclastic layer. The cemented cataclasite evolves in a fault breccia with an exponential decrease in damage into the protolith. (c) Slabbed core, drilled perpendicular through the fault zone (from Collettini et al., 2014). The foliated cataclasite (FC) shows hydrofractures and pressure solution seams. The footwall block is mainly characterized by 2–10 cm thick cemented cataclasite (CC) and by a thicker (up to few meters) highly fractured fault breccia (FB) shading into the protolith.

wear striae, circular cracks, and comb fractures (Collettini et al., 2014a; Tesei et al., 2017) as shown in Figures 2a and 2b.

In the hanging-wall block, fault rock derived from a calcareous-marly protolith (91.7% carbonate and 8.3% clay), is represented by a carbonate-rich foliated cataclasite (Figure 2c, left), where clay-rich pressure solution seams (stylolites) and calcite-rich veins with mutual crosscutting relationships are observed. These structural features indicate that during fault activity, deformation processes such as cataclasis, pressure solution, and hydrofracturing with cementation were active in the slip zone of the hanging-wall block (Collettini et al., 2014a).

Moving away from the slip surface, the footwall block is characterized by a thin zone, $<$2 cm, of ultracataclasite (see Carpenter et al., 2014, and Collettini et al., 2014a, for details) followed by a 2–10 cm thick cataclastic layer and fault breccia (Figure 2c). Both the ultracataclasite and cataclasite form from the CM formation. The cataclasite layer has a thickness ranging from a few centimeters to about 10 cm and is characterized by a fine-grained texture with a few principal slip surfaces and calcite veins. One prominent feature of this layer is its strong cohesion, likely related to cementation processes (healing and sealing) that occurred within the fault zone. Fault breccia (Figure 2c, right) is represented by clasts of calcare massiccio separated by visible open fractures, calcite-rich veins and limited pressure solution seams with fractures that often reopen preexisting calcite-filled cracks. A characteristic of fault breccia is larger clast dimensions in comparison to the cataclasite and ultracataclasite layers. In some portions of the slip zone, Collettini et al. (2014a, 2014b) documented small displacement ($<$1 cm) fault planes both synthetic and antithetic to the major slip surface that merge into it.

2.1. Investigated Samples

We collected large cores (100 mm in diameter and up to 20 cm in length), drilled perpendicular to the fault plane (Figures 2b and 2c). These cores were then subsampled to obtain smaller cores (38 mm in diameter and 38 mm in length). Following the fault zone architecture described above, we classified the fault rock samples as: foliated cataclasite (FC in Figure 2c) that represents the clay-rich domain of the fault core, cemented cataclasite (CC in Figure 2c) or the carbonate-rich fault core, and fault breccia (FB in Figure 2c) or the damage zone. For comparison, we also collected samples from the protolith (P).

Optical microscope analyses of the clay-rich domain displays a cataclasite with abundant pressure solution surfaces and calcite-rich veins, in agreement with mesoscale observations. Microcracks are also present with orientations that seem to follow both grain boundaries and pressure solutions seems (Figure 3a).

The cemented cataclasite consists of randomly oriented, subcentimetric angular clasts of calcare massiccio formation, dispersed within a fine-grained calcite-rich ground mass (Figure 3b). Microcracks between clasts are abundant whilst very few open cracks and pressure solution seams are present.

The footwall fault breccia shows a high variability of clast dimensions ranging from a few microns to some centimeters. Open cracks that often reopen preexisting calcite-filled cracks are the prominent features of this portion of the fault footwall block (Figure 3c).

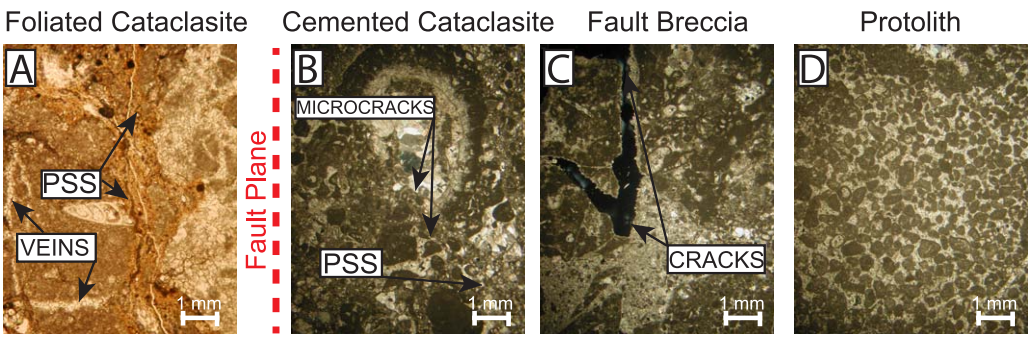

Figure 3. Representative microstructures of the test samples from thin sections: (a) Foliated and clay-rich cataclasite located in the hanging-wall of the fault plane with abundant calcite-filled veins, and pressure solution surfaces (bottom inset). (b) Cemented cataclasite with submillimiter-scale clasts and abundant microcracks. (c) Fault breccia showing clasts with variable dimensions, and abundant open cracks. (d) Protolith (calcare massiccio limestone) showing the undeformed classical oolitic grainstone texture.

The protolith shows the typical oolitic grainstone microscopic textures of the calcare massiccio limestone (e.g., Santantonio, 1994). At the microscale, this tight limestone is characterized by the absence of cracks, microcracks, and pores (Figure 3d).

3. Experimental Methodology

We tested 16 cylindrical core samples representative of the main structural domains of the fault (Figure 2), i.e., clay-rich foliated cataclasite (FC), cemented carbonate-bearing cataclasite (CC), fault breccia (FB), and the protolith (P). For all the samples, we measured density, porosity, and *P* and *S* wave velocity at ambient pressure under dry conditions. Seismic wave velocities were also measured at effective confining pressures ranging up to 100 MPa. All experiments were performed at the HP-HT Laboratory of Experimental Volcanology and Geophysics of the Istituto Nazionale di Geofisica e Vulcanologia in Rome (Italy). Samples consist of

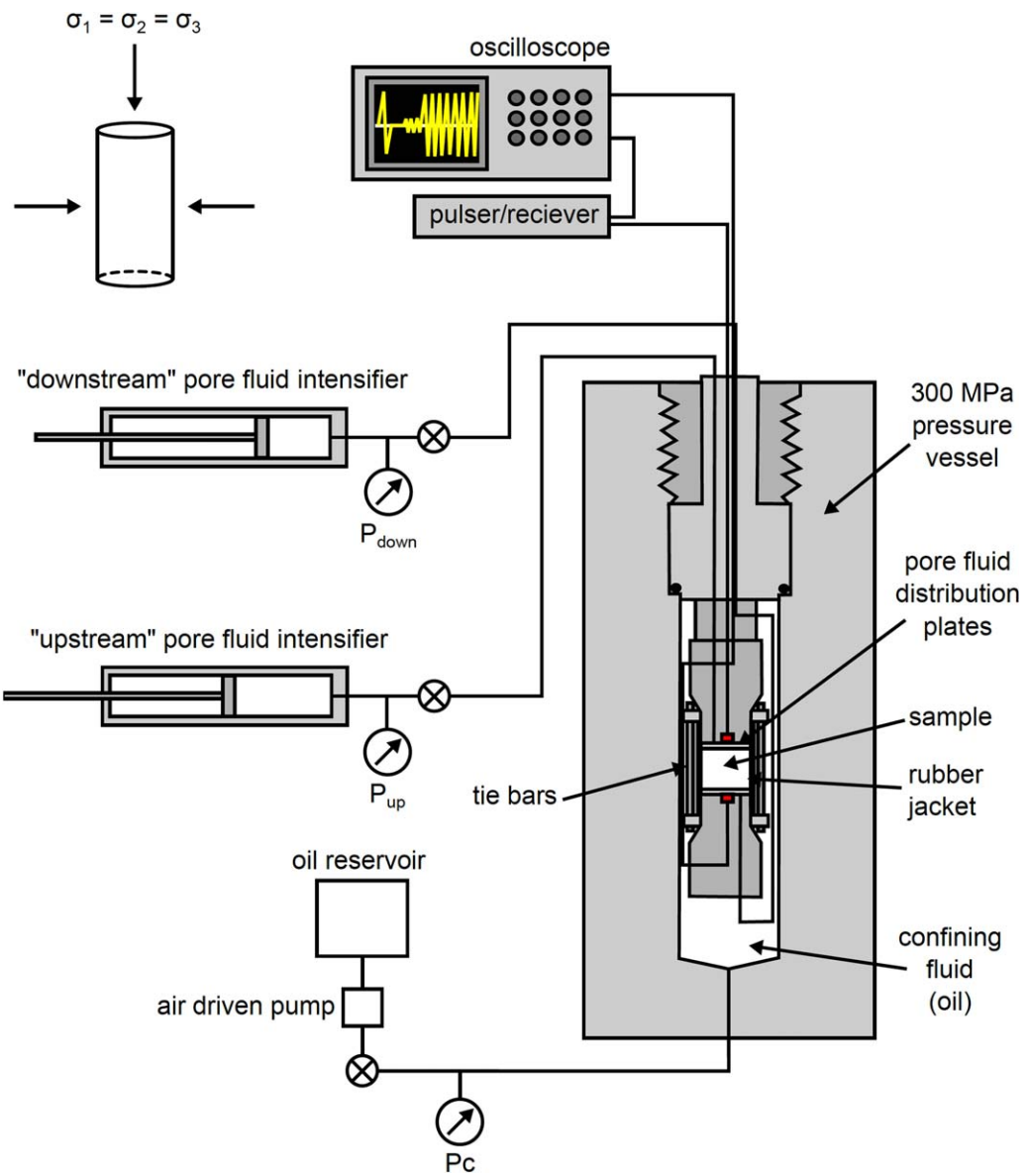

Figure 4. Schematic diagram (from Heap et al., 2014b) of the servo-controlled permeameter equipped for measurements of V_p, V_s, and permeability up to confining pressures of 100 MPa at the High Pressure High Temperature (HPHT) Laboratory, Istituto Nazionale di Geofisica e Vulcanologia (INGV), Rome. The sample size is 38 mm in diameter and 38 mm in length.

cylinders, 38 mm in diameter and 38 mm long, with their end faces ground flat and parallel to ±0.02 mm. Density measurements were performed on samples that had been dried in an oven at 60°C for a minimum of 24 h. This modest temperature is used to preclude any possibility of thermal cracking in the samples prior to measurement (Fredrich & Wong, 1986; Glover et al., 1995). The porosity for each sample was measured using a helium pycnometer (AccuPyc II 1340) with an analytical accuracy of ±0.001%. Initial elastic wave velocity measurements were made axially on dry samples under ambient laboratory conditions using the pulse transmission technique (Birch, 1960, 1961). A 900 V pulse generator was used to excite a 1 MHz resonant frequency piezo-electric transmitting transducer, and the resulting waveforms were recorded using an identical receiving transducer. After preamplification, signals were recorded and displayed on a digital storage oscilloscope.

Experiments under fluid-saturated conditions were performed using a standard permeameter (Figure 4) that is equipped with three servo-controlled pressure intensifiers used to apply a confining pressure (P_c), up to 100 MPa, and an upstream and downstream pore fluid pressure (maximum pressure 70 MPa). Confining pressure is applied using a hydrogenated paraffinic oil. For pore fluid, we used a calcium-rich water solution similar to the water circulating in carbonate-bearing faults. For the configuration of the testing apparatus, the confining pressure is applied isotropically to the sample (i.e., $\sigma_1 = \sigma_2 = \sigma_3$) and the effective stress results from $\sigma_{eff} = P_c\text{-}P_f$, where P_f is the fluid pressure. The sample assembly consists of two end-caps that sandwich the cylindrical core sample. Each end-cap is equipped with two 1 MHz resonant frequency piezo-electric transducers crystal, one for compressional (V_p) and one for shear (V_s) wave velocity measurements. During each experiment, we increased the effective pressure in steps of 10 MPa, under hydrostatic boundary conditions, until a maximum effective pressure of 100 MPa. For each pressure step, we measured axial *P* and *S* wave velocity and sample permeability. The accuracy of the *P* and *S* wave velocity is estimated as 1–2% for V_p and 2–4% for V_s. Sample permeability was measured by applying a constant head method that consist in applying a differential fluid pressure between the upstream and downstream reservoir (2 MPa for all measurements reported here) and measure the resulting flow rate. We subsequently determined sample permeability from the measured flow rates and the sample dimensions, by direct application of Darcy's law.

Table 1
Summary of the Physical Properties of the Fault Rocks Samples Measured at Ambient Pressure

Sample	Bulk density (g/cm^3)	Total porosity (%)	Eff. porosity (%)	V_p (km/s)	V_s (km/s)	V_p/V_s
P01	2.66	7.4	1.7	6.12	3.19	1.92
P02	2.67	6.9	1.3	6.16	3.26	1.89
P03	2.66	7.1	1.4	6.53	3.20	2.04
P04	2.69	6.3	0.5	6.65	2.60	2.56
P05	2.68	6.4	0.7	6.13	2.84	2.16
Average P	**2.67**	**6.8**	**1.1**	**6.32**	**3.02**	**2.11**
FB01	2.53	11.6	6.3	4.59	2.95	1.56
FB02	2.47	13.8	12.9	5.55	2.68	2.07
FB03	2.50	12.7	2.5	5.77	2.78	2.08
FB04	2.57	10.2	4.6	5.21	2.91	1.79
FB05	2.58	9.9	4.4	4.90	2.67	1.84
FB06	2.52	12.1	6.7	5.53	2.47	2.24
Average FB	**2.53**	**11.7**	**6.2**	**5.26**	**2.74**	**1.93**
CC01	2.61	9.1	3.6	5.41	2.62	2.07
CC02	2.62	8.7	3.1	5.97	2.87	2.08
CC03	2.60	9.2	3.7	5.63	2.56	2.20
CC04	2.61	9.0	3.5	5.62	2.71	2.07
Average CC	**2.61**	**9.0**	**3.5**	**5.66**	**2.69**	**2.10**
FC01	**2.65**	**7.7**	**2.4**	**4.38**	**2.66**	**1.65**

Note. Bold line indicates the average values of each fault rock type. Eff. porosity is connected porosity, V_p is *P* wave velocity, V_s is *S* wave velocity where their ratio is reported in the last column

4. Results

4.1. Measurements at Ambient Pressure

In this section, we report results from measurements of bulk density, porosity, and axial *P* wave velocity made at ambient pressure (0.1 MPa): these results are listed in Table 1.

By averaging the values of each fault rock type (Table 1, bold) it results that the protolith, *P*, has an average porosity of 6.8%, formed predominantly by isolated pores since the connected porosity is only 1.1%. These values are in good agreement with microstructural observations and previous measurements on similar tight limestones (e.g., Agosta et al., 2007; Mavko et al., 2009). FB samples are characterized by the highest bulk porosity (11.7%) and a resulting connected porosity of 6.2%, whilst CC samples show lower bulk porosity (9.0%) and a connected porosity of 3.5%. It is worth noting that FB samples show a relatively wide range of both total (from 13.8% to 9.9%) and connected (from 12.9% to 2.5%) porosity values in comparison to CC samples that possess a narrow porosity range. The high heterogeneity of FB samples is related to the highly variable dimensions of the clasts observed at the microscale (from microns to some centimeters). The clay-rich cataclasite shows a bulk porosity of 7.7% and a connected porosity of 2.4%, both values being slightly lower with respect to CC samples.

Measured density values (2.47–2.69 g/cm^3) are those typical for limestones (Mavko et al., 2009) where higher density is linearly related to lower porosity. Variations in density can, in fact, be only related to

variation in porosity, in particular for pure limestone (CC, FB and P) samples, since no bulk mineralogical differences have been observed between these samples.

Axial *P* wave (V_p) and *S* wave (V_s) velocities measured at ambient pressure are listed in Table 1. The highest V_p values were recorded for the protolith samples (average $V_p = 6.32$ km/s) whereas CC velocities (average $V_p = 5.66$ km/s) are generally higher than FB velocities (average $V_p = 5.26$ km/s). The higher velocities recorded for protolith samples are consistent with microstructural details showing higher density, lower porosity, and absence of cracks.

The clay-rich foliated cataclasite (FC) is characterized by the lowest velocity ($V_p = 4.38$ km/s), likely related to (1) the more marly protolith, and (2) the presence of the abundant pressure solution seams, often reopened by microcracks almost perpendicular to the wave propagation direction.

The V_p/V_s ratios follow the same trend of V_p values being higher for protolith samples (2.11) and slightly lower for CC samples (2.10 on average). FB samples show the lower V_p/V_s ratio for footwall rocks (1.93) while the lowest value of the data set has been recorded for the FC samples (1.65).

4.2. Measurements at Elevated Pressure

V_p and V_s measurements were made on dry samples during pressurization from 0.1 to 100 MPa in 10 MPa increments, and during depressurization back to ambient pressure.

The results show that the velocities during pressurization and depressurization cycles are essentially similar, within measurement accuracy, and therefore the velocity hysteresis is negligible for all the tested samples with the exception of some FB samples. This suggests that, during pressurization, inelastic compaction acted only in FB samples. Since FB samples are highly fractured, as confirmed by high porosity at ambient pressure (Table 1) they are prone to compaction due to crack closure induced by pressurization. Due to this general absence of significant hysteresis, and for simplicity, we report only velocity measurements made during depressurization (Burke, 1987).

Variations in *P* and *S* wave velocity for dry samples as a function of the effective pressure are shown in Figure 5. All samples exhibit higher velocities at higher pressures, i.e., >40 MPa, due to the closure of cracks and the consequent decrease in porosity. Within this general trend, we observe that FB samples show a larger variability in velocities: 4.5–5.5 km/s at ambient pressure and 5.5–6 km/s at 100 MPa confining pressure. These samples also show the largest V_p increase: about 20% recorded within the first 40 MPa of applied confining pressure. Velocities are more pressure independent for the other rocks type, and absolute values show a narrower range (Figure 5). In particular, this trend is evident for CC and P samples (see Table 1) coherently with their meso-microstructural and petrophysical characteristics that show very low porosity, which is mostly not connected, i.e., primary porosity that is pressure independent. Moreover, the internal structure is homogeneous for all CC and P samples resulting in similar physical properties, which explains the recorded narrow range of velocities within these two groups. Clay-rich pressure solution seams are abundant in the foliated cataclasite (FC), decreasing the absolute velocities in respect to the pure limestone protolith. This effect is particularly evident at higher confining pressure where FC and P samples show a V_p of ~4.7 and 6.2 km/s, respectively, resulting in a difference of 1.5 km/s.

For FB samples, the V_P/V_s ratio shows a large range, $1.95 < V_p/V_s < 2.15$, even at elevated pressures, whilst the other lithologies are more homogeneous resulting in a narrower range of V_p/V_s (red curves on Figure 5). For all the samples investigated, the evolution of the V_p/V_s ratio show a slight decrease at low confining pressures and becomes pressure independent above ~30 MPa, in agreement with observations conducted on similar rock types such as dolomites (Trippetta et al., 2010).

Permeability measurements on water-saturated samples were performed at a constant pore fluid pressure (P_p) of 10 MPa. Since the applied confining pressure (P_c) must be equal to or greater than P_p, this means that measurements were necessarily conducted in the range of effective pressure, ($P_e = P_c - P_p$) between 10 and 100 MPa. The clay-rich foliated cataclasite shows the lowest permeability (Figure 6) with a pressure-independent value of about 6×10^{-19} m^2. This value is related to the presence of abundant clay-rich pressure solution seams arranged perpendicular to the fluid flow. Similar values of permeability have been recorded for the protolith, where the coupling between the very low porosity and the absence of fractures results in a very low permeability for this lithology. Our data are in agreement with those from Heap et al. (2014a) showing that when the fluid flow direction is perpendicular to pressure solution structures such as stylolites, the permeability is similar to that of the undeformed material.

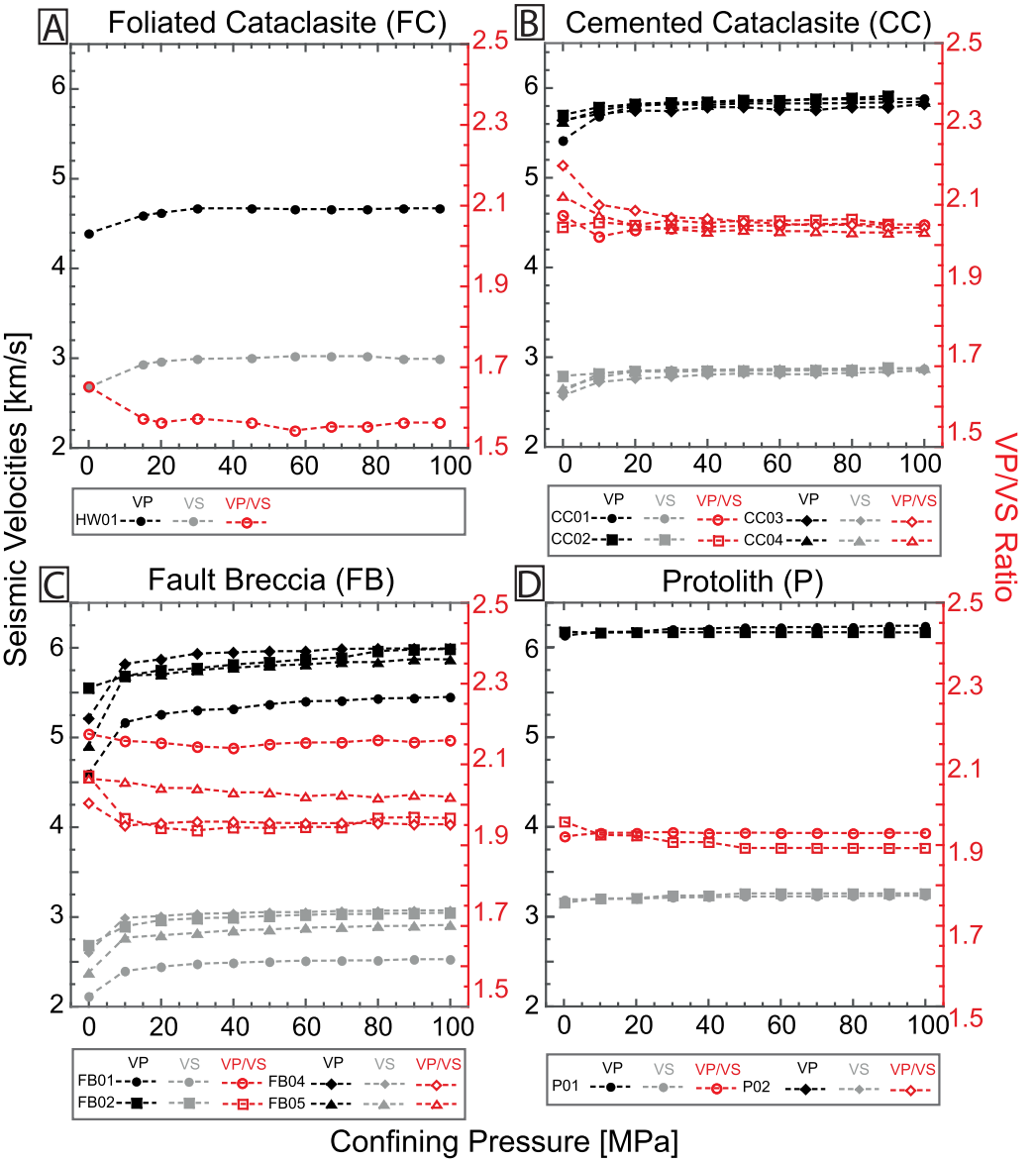

Figure 5. Variation in axial *P* wave velocity (black), *S* wave velocity (grey), and V_p/V_s ratio (red) as a function of the effective confining pressure for all fault rocks: (a) foliated cataclasite; (b) cemented cataclasite; (c) fault breccia; and (d) footwall protolith.

Permeability of the CC sample ($\sim 4 \times 10^{-18}$ m^2) is higher than the protolith P ($\sim 6 \times 10^{-19}$ m^2) and it is pressure independent. In contrast, the permeability of the FB sample is higher and pressure dependent showing values that decrease from $\sim 2 \times 10^{-16}$ m^2 at ambient pressure to $\sim 2 \times 10^{-17}$ m^2 at 100 MPa of confining pressure (Figure 6).

4.3. Elastic Moduli

In order to assess the influence of the different structural domains of the fault zone on elastic moduli, we determined Young's modulus (E_d) and Poisson's ratio (ν_d) values for each fault rock (P, FB, CC, and FC) at 0.1, 10, and 100 MPa. The dynamic moduli (E_d and ν_d) were calculated from measurements of V_p and V_s using the equations:

$$E_d = \rho \frac{V_s^2\left(3V_p^2 - 4V_s^2\right)}{V_p^2 - V_s^2} \quad (1)$$

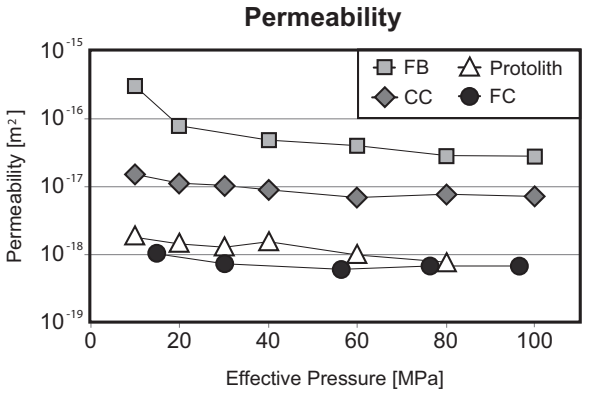

Figure 6. Variation of permeability with increasing effective pressure up to 100 MPa for clay-rich foliated cataclasite (FC, circles), cemented cataclasite (CC, diamonds), fault breccia (FB, squares), and footwall protolith (P, triangles).

$$v_d = \frac{1}{2}\frac{V_p^2 - 2V_s^2}{V_p^2 - V_s^2} \quad (2)$$

where ρ is rock density and V_p and V_s are the compressional and shear elastic wave velocities, respectively. Results are summarized in Table 2. As the confining pressure increases, the Young's modulus (E_d) increases and the Poisson's ratio (v_d) decreases (Figure 7), in agreement with similar data previously reported in the literature (Heap & Faulkner, 2008). The protolith exhibits the highest Young's modulus and the lowest Poisson's ratio of the footwall rocks. Within the fault zone E_d values are lower in FB than in CC. However, this difference vanishes with increasing confining pressure (Figure 7). This highlights the important role played by the open fractures, contained within FB, in controlling E_d at low confining pressure in agreement with previous data on similar fractured rocks (Trippetta et al., 2013b). Dynamic Poisson's ratio is higher for FB with respect to CC indicating that the tested FB samples are weaker (more radially deformable) than CC samples. This is particularly true at low confining pressure due the presence of a great number of cracks (see Figure 3 and section 2). In general, from the fault breccia to the cemented cataclasite, Young's modulus decreases and Poisson's ratio increases, with a nonlinear trend. For the clay-rich foliated cataclasite, E_d is in the range of FB and CC values whereas v_d is significantly lower. This could be related to several factors including: (1) the different protolith (see section 2) and (2) the presence of many pressure solution seams resulting in a strong anisotropy of the sample. In addition, due to the impossibility of obtaining samples parallel to the foliation, we have been able to test only samples drilled perpendicularly to the foliation. By measuring velocity perpendicular to the fault plane V_p tends to decrease due to the presence of several discontinuities that affect V_p more than V_s. For this reason, we observe a reduction in both E_d and v_d values with respect to the footwall fault rocks.

5. Discussion

5.1. Evolution of Fault Zone Physical Properties During Deformation

The petrophysical characterization of distinct carbonates rocks that are representative of different structural domains of a fault zone allowed us to draw a quantitative picture of the processes acting on a carbonate-bearing fault.

Porosity variations measured between P, FB, and CC samples suggests that starting from the protolith, fracturing would increase both the total porosity (from ~7% to ~12%) and the connected porosity (from ~1% to ~6%); thus, new pores with high aspect ratio should form during this process. Accordingly, permeability of FB samples is higher, V_p is lower with respect to the protolith, and both are pressure dependent. Once the FB is formed, cataclasis and grain size reduction acting near the fault plane, together with healing and sealing processes, would tend to decrease porosity, both total (from ~12% to 9%) and connected (from ~6% to 3.5%), producing the cemented cataclasite, CC. These microstructural changes within the CC are highlighted by the lower permeability values and higher V_p velocities with respect to FB samples (Figures 5 and 6); in addition, permeability and V_p are pressure independent. The pressure dependency of permeability for FB (Figure 6) highlights that cracks tend to close at relatively low confining pressure (i.e., above 40 MPa). However, this crack closure is not enough to inhibit the role of fractures in increasing permeability, making FB the structural domain where crustal fluids can easily flow, even at seismogenic crustal depths (4–8 km). To be noted that our laboratory results are applicable to the current state of cementation within the fault zone, while the state of cementation may vary during the seismic cycle. Results from previous laboratory studies indicate that the permeability of similar carbonate-fault rocks ranges from 10^{-16} to

Table 2
Measured Mechanical Properties (Young's Modulus, YM, and Poisson's Ratio, PR) of the Tested Samples at 0.1, 10, and 100 MPa of Confining Pressure

	YM (GPa)	PR	YM (GPa)	PR	YM (GPa)	PR
Sample	0.1 MPa	0.1 MPa	10 MPa	10 MPa	100 MPa	100 MPa
P01	65.47	0.32	65.52	0.32	68.42	0.32
P02	67.65	0.32	69.28	0.32	71.27	0.31
Average P	**66.56**	**0.32**	**67.40**	**0.32**	**69.85**	**0.31**
FB01	39.26	0.35	53.15	0.34	58.37	0.34
FB02	47.83	0.35	54.68	0.33	60.63	0.33
FB04	46.44	0.33	60.67	0.32	64.12	0.32
FB05	30.84	0.37	39.59	0.36	43.99	0.36
Average FB	**41.10**	**0.35**	**52.02**	**0.34**	**56.78**	**0.34**
CC01	47.87	0.35	55.19	0.34	57.61	0.34
CC02	54.61	0.34	55.75	0.35	58.41	0.34
CC03	46.98	0.37	52.04	0.35	56.74	0.34
CC04	50.38	0.36	54.76	0.35	58.58	0.34
Average CC	**49.96**	**0.35**	**54.43**	**0.35**	**57.84**	**0.34**
FC01	**45.29**	**0.21**	**52.31**	**0.16**	**54.32**	**0.15**

Note. Bold line indicates the average values of each fault rock type.

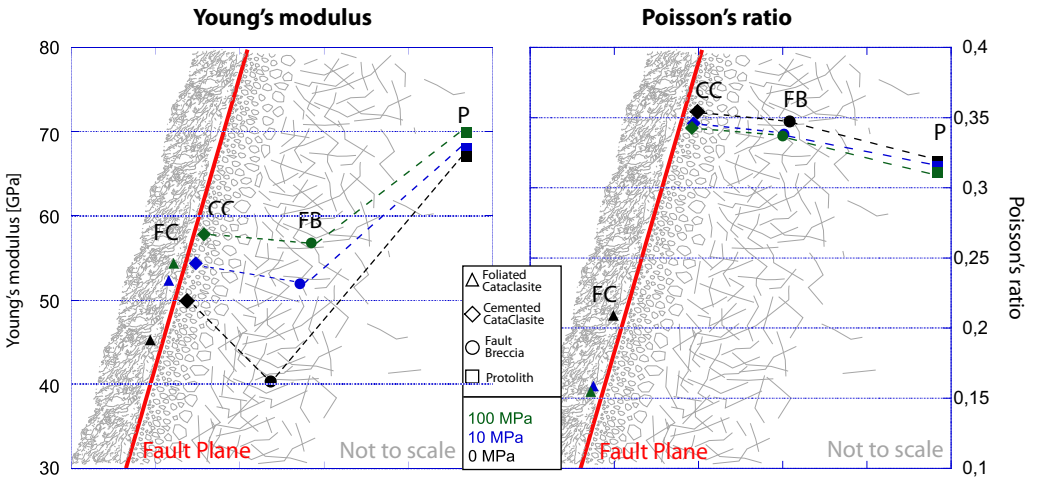

Figure 7. Variation of (a) Young's modulus and (b) Poisson's ratio as a function of the fault zone architecture. The elastic parameters of foliated cataclasite (FC, circles), cemented cataclasite (CC, diamonds), fault breccia (FB, squares), and protolith (P, triangles) are reported at effective pressures of up to 0.1 MPa (black), 10 MPa (blue), and 100 MPa (green).

10^{-20} m^2 at effective pressure up to 50 MPa, depending on fault rock type (Agosta et al., 2007). Our results are in agreement with these data, showing permeability down to 10^{-19} m^2 for undeformed rocks and up to 10^{-16} m^2 for the most intensely fractured rocks (FB). Permeability of granular fault gouges, obtained from crushing and sieving a protolith similar to the one analyzed here, show values in the range of 5×10^{-17}–7×10^{-18} m^2 (Scuderi & Collettini, 2016).

The tested clay-rich foliated cataclasite is affected by different deformation mechanisms as shown by numerous pressure solution seams with clay concentration along the stylolites. This fabric leads to lower the permeability (1×10^{-18}–9×10^{-19} m^2) and porosity, and a reduction in *P* wave velocities, which influences the elastic parameters and hence, the mechanical behavior of this portion of the fault zone.

5.2. Comparison Between Laboratory-Scale and Field-Scale *P* Wave Measurements

We have estimated synthetic *P* wave sonic logs profiles as a function of depth (Figure 8) by (1) supposing a general lithostatic stress gradient of 25 MPa/km, and (2) reporting the recorded values of *P* wave velocities of carbonate samples analyzed in this work (CC, FB, and P): V_p of FB (FB01 sample, cf. Table 1) represents the lower boundary of the synthetic profile whilst V_p of the P01 sample (Table 1) marks the upper boundary. These data, derived from the laboratory experiments, have been compared with digitalized *P* wave sonic logs from three boreholes that drilled the calcare massiccio FM in Italy: Daniel1, Monte Civitello1, and Varoni1 (http://unmig.sviluppoeconomico.gov.it/videpi/videpi.asp). Figure 8 shows shows the relationship between the synthetic profile and the sonic log profiles reported in the boreholes composite log; the three boreholes locations are reported in Figure 1. In the laboratory versus in situ comparison, we report only the sonic log data for those portions of the wells that passed through the calcare massiccio formation and laboratory data from footwall samples since they pertain to the same formation (cf. also section 2). All of the reported sonic logs are highly scattered as commonly observed for similar measurements and for data acquired in the 1980s (e.g., Latorre et al., 2016; Smeraglia et al., 2014; Trippetta et al., 2010, 2013). This is due to technical issues related to the acquisition tool and fluctuations of fluid pressures during the acquisition, thus anomalous high or low velocities can be considered as biased. The Daniel1 well penetrated the calcare massiccio formation from about 1,750 to 2,015 m depth, and the lithology consists of highly fractured, pure limestone. The sonic log indicates a V_p in the range of 5.8 to 6.2 km/s. Recorded velocities mostly fall in the laboratory range whilst spikes in the upper part of the log indicates lower velocities. The Monte Civitello1 well-encountered calcare massiccio formation over the depth range 2,250–2,700 m. The composite log highlights the presence of Packstone-Wackestone (Dunham, 1962) textures for the whole interval. Recorded values range from 4.0 to 7.5 km/s particularly in the depth range 2,450–2,600 m, however, most values fall between 5.5 and 6.2 km/s. In agreement with Daniel1 data, *P* wave velocities are mostly consistent with laboratory results.

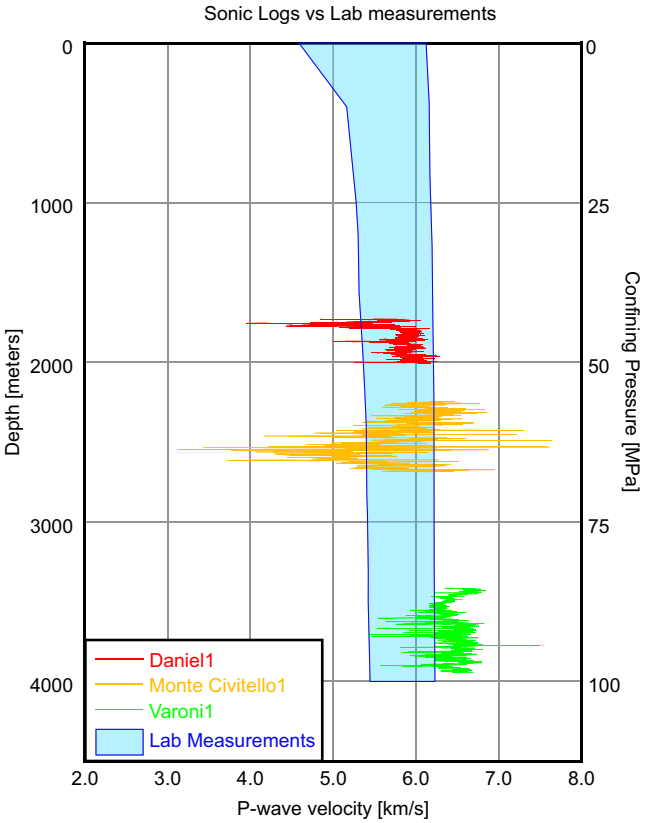

Figure 8. Comparison between synthetic V_p depth profile derived from the laboratory *P* wave velocity measurements reported in this study and in situ V_p measurements from sonic logs through the calcare massiccio (http://unmig.sviluppoeconomico.gov.it/videpi/videpi.asp). See text for details of the method used for the calculation of the synthetic profile.

The Varoni 1 well penetrated the calcare massiccio formation from 3,418 to 4,400 m, where dolomitized Packestone-Grainstone textures are reported in the composite log for this interval. The sonic log records stop at depth of 3,947 m due to technical problems, for this reason we report V_p in the interval 3,418–3,947 m. V_p recorded on this well are mostly in the range 6.1–6.8 km/s. These velocities are higher with respect to what we recorded in the laboratory and higher with respect to any laboratory value for pure carbonates (e.g., Mavko et al., 2009).

The comparison of velocity data from sonic logs and laboratory measurements shows that most of the sonic log data agree with laboratory measurements. Moreover, both lab and in situ data clearly show that for the calcare massiccio formation the confining pressure (depth) does not influence velocity at the investigated depths. In addition, in situ data show some lower velocities with respect to laboratory measurements. This can be well explained by the presence of in situ mesoscale fractures not reproducible in laboratory (Trippetta et al., 2013a; Vinciguerra et al., 2006). For the Varoni1 borehole, we also observed the unusual situation of higher in situ velocities with respect to laboratory measurements. However, these higher in situ velocities are associated with a dolomitized portion of the calcare massiccio formation. The dolomitization of a pure limestone can progressively increase its initial velocity (Mavko et al., 2009) up to 7.3 km/s (Trippetta et al., 2010). On the other hand, mesoscale fracturation can reduce V_p values down to the observed values at the Varoni1 well (average $V_p \sim 6.7$ km/s). We then suggest that both physical (mesoscale fractures) and chemical (dolomitization) processes are crucial for the propagation of seismic waves in carbonates at crustal scales. In general, the agreement between laboratory and in situ data indicates that the elastic moduli derived from laboratory V_p measurements represent a good estimate for the elastic properties of natural carbonate-bearing fault zone structures at seismogenic crustal levels.

5.3. Implications for Earthquake Nucleation on Carbonate-Bearing Faults

Once a fault has been formed, its further motion and slip behavior, seismic or aseismic, is controlled by the frictional properties of the sliding surface and the elastic properties of the medium surrounding the fault. In this paragraph, we integrate our data on Elastic moduli (the fault surrounding medium) with fault frictional properties derived from the literature, to discuss earthquake nucleation on carbonate-bearing faults.

Earthquake nucleation and the mechanics of frictional sliding can be evaluated for a 1-D fault obeying rate- and state-friction (Dieterich, 1979; Marone, 1998; Ruina, 1983) by considering the elastic stiffness of the surrounding medium, k, and the fault frictional properties, which can be written in terms of a critical rheologic stiffness k_c (Gu et al., 1984). The condition for instability, when sliding velocity is still low, can be written as:

$$k < k_c = \frac{(\sigma_n P_f)(b-a)}{D_c} \tag{3}$$

where σ_n is the normal stress, P_f is the pore fluid pressure, $(b-a)$ is the friction rate parameter, and D_c is the critical slip distance. Numerical studies (Gu et al., 1984) and recently laboratory data (Ikari et al., 2015; Leeman et al., 2016; McLaskey & Yamashita, 2017; Scuderi et al., 2016) confirmed the theoretical criterion of equation (3). For a two- or three-dimensional case, the stiffness k must be inversely proportional to a length scale (Kanamori & Brodsky, 2004; Scholz, 2002). If the slipping region is treated as an elliptical crack, the stiffness k is:

$$k = \frac{E}{2(1-\nu^2)L} \tag{4}$$

where L is the length of the slipping region, E is the Young's modulus, and ν is the Poisson's ratio. Combining equation (3) with equation (4) results that the stability transition occurs at a critical length of the slipping region, L_c, given by:

$$L_c = \frac{ED_c}{(1-\nu^2)\sigma_n(b-a)} \tag{5}$$

Equation (5) predicts that stable sliding will occur during a nucleation stage until the slipping region grows to L_c and then, the earthquake instability occurs.

To evaluate L_c for carbonate-bearing faults, we used the elastic moduli of the Monte Maggio Fault, i.e., CC and FB that represent the fault loading medium (paragraph 4.3). The effective pressures of the laboratory

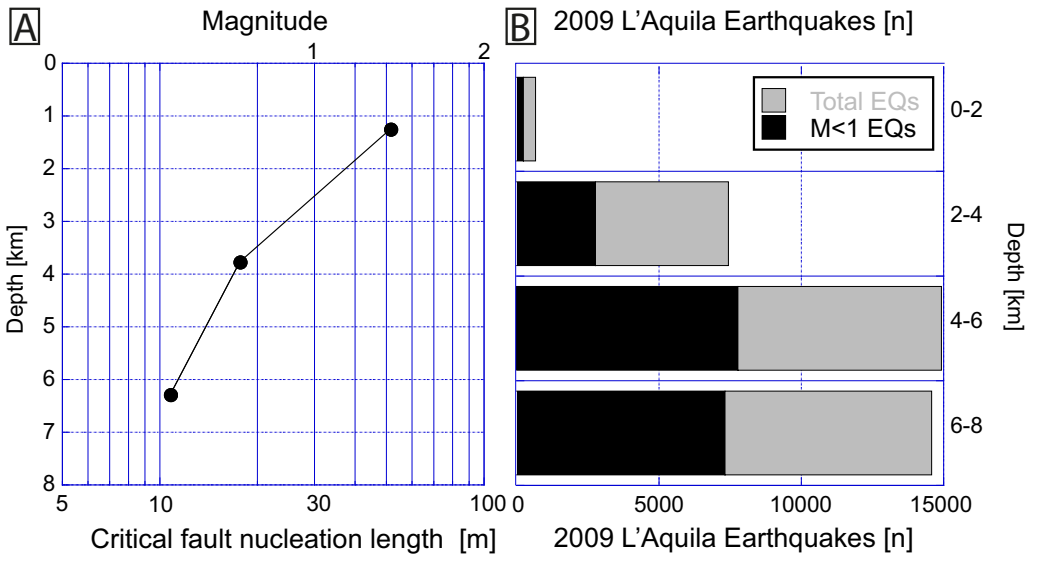

Figure 9. Comparison between: (a) the calculated critical nucleation length L_c with increasing depth (horizontal axis reported the critical nucleation length, L_c, and the equivalent minimum earthquake magnitude, M) and (b) the totale (grey) and $M \leq 1$ (black) earthquake depth-distribution of the 2009 L'Aquila sequence (Chiaraluce et al., 2011) showing an increase of both total and $M < 1$ earthquakes above ~4 km.

Table 3
Imposed Confining and Fluid Pressures With Corresponding Depths and Normal Stresses, Used in Equation (5) to Calculate L_c of Figure 9a

Confining pressure (MPa)	Pore fluid factor	Equivalent depth (m)	Sigma n (MPa)	YM (GPa)	PR	D_c (m)	b−a (m)
20	0.4	1258	10	54.72	0.3406	0.00005	0.003
60	0.4	3775	30	56.36	0.3396	0.00005	0.003
100	0.4	6292	50	57.31	0.3398	0.00005	0.003

Note. Young's Modulus (YM) and Poisson's Ratio (PR) at respective confining pressures have been obtained by averaging FB and CC data from this work. The values of 0.003 for b-a represents an average respect to the range of 0.001–0.006 reported in literature (Carpenter et al., 2016; Collettini et al., 2014a; Verberne et al., 2010, 2015). Similarly D_c value of 50×10^{-6} m represent an average respect to the range of 10×10^{-6}–100×10^{-6} m derived from previous works (Carpenter et al., 2014; Scuderi & Collettini, 2016).

experiments have been converted to crustal depths assuming a hydrostatic fluid pressure represented by a pore fluid factor of $\lambda = P_f/\rho gz = 0.4$, where ρ is the rock density, g is the acceleration due to gravity, and z is the crustal depth. For the frictional properties, we used data from the Monte Maggio Fault (Carpenter et al., 2014) and other data on carbonates at different boundary conditions (Carpenter et al., 2016; Scuderi et al., 2016; Verberne et al., 2010, 2015). The data used to estimate L_c (Figure 9a) are reported in Table 3. The L_c values evolve from about 50 m at shallow crustal levels to 12 m below 6 km. This is a rough estimate of L_c that can increase or decrease based on changes in the different parameters of equation (5). In particular, a reduction of D_c induced by fluid overpressure (Scuderi & Collettini, 2016) can reduce L_c as well as a more pronounced velocity weakening behavior favored by the increase of temperature (Verberne et al., 2010, 2015). On the other hand, a less pronounced velocity weakening behavior at low normal stresses (Carpenter et al., 2016) or due to fault rock heterogeneities (Carpenter et al., 2014) favors an increase L_c. Taking into account the variability mentioned above, the analysis on L_c suggests that: (1) within the seismogenic layer, earthquake occurrence should increase with depth since L_c decreases (Figure 9); (2) at shallow crustal levels, $M \leq 1$ earthquakes are unlikely since the critical nucleation length is larger than the earthquake rupture radius estimated from elastic dislocation theory considering the fault as a circular crack with a stress drop of 3 MPa (Kanamori & Anderson, 1975; Sibson, 1989). To test these hypotheses, in Figure 9b, we have reported the frequency-depth distribution of total earthquakes and those with magnitudes $M \leq 1$ recorded during the 2009 L'Aquila seismic sequence (Chiaraluce et al., 2011) that occurred on carbonates similar of those tested in this study (Valoroso et al., 2014). The increase of earthquake occurrence with depth agrees with the reduction of L_c with depth. The reduction of the percentage of earthquakes at shallow crustal levels is consistent with the mechanical prediction that L_c is larger than the dimension of a $M \leq 1$ earthquake at such a depth. In addition, the presence of $M \leq 1$ at shallow crustal levels can be addressed by several factors including the mentioned variations in the rate and state friction parameters that would reduce L_c and stress transfer processes induced by the larger events (e.g., Boatwright & Cocco, 1996; Stein et al., 1992).

6. Conclusions

Physical and transport properties of the investigated fault zone are controlled by the different deformation processes. Fracturing in the fault breccia results in high porosity (11% total and 6.2% connected), low and pressure-dependent V_p (4.9–5.9 km/s), and relatively high and pressure-dependent permeability (10^{-16}–10^{-17} m^2). Grain size reduction and cementation process near the fault plane reduce porosity (9% total and 3.5% connected), increase V_p (5.9 km/s), and decrease permeability (9×10^{-18} m^2). Fault rocks affected by pressure solution processes show significantly different physical properties: low porosity (7.7% total and 2.4% connected), low V_p (4.4 km/s), and low permeability (8×10^{-19} m^2).

The comparison between laboratory V_p measurements and with in situ sonic logs shows a general agreement for the two data sets. Lower in situ P wave velocities (~5 km/s at 2,500 meters in the M. Civitello1 borehole) in comparison to laboratory measurements (5.5–6.2 km/s at equivalent depth) are likely related to mesoscale fractures that cannot be captured in experiments conducted on centimeter samples. Higher in situ P wave velocities (~6.5 km/s at 3,800 m in the Varoni1 borehole) in comparison to laboratory measurements (5.5–6.2 km/s at equivalent depth) can be explained by the dolomitization documented in the borehole report.

The characterization of the fault critical nucleation length, L_c, obtained from elastic moduli and frictional properties suggests that at shallow crustal levels, $M \leq 1$ earthquakes are less favored, since the critical nucleation length is larger than the earthquake rupture radius. Considering the influence of the frictional parameters in estimating L_c at first approximation, our results are consistent with the small number of $M \leq 1$ earthquakes recorded at shallow crustal depth during the L'Aquila 2009 seismic sequence occurring on carbonates.

Acknowledgments
F. Trippetta and M. M. Scuderi were supported by Progetti di Ateneo (Sapienza) 2016 "From small to large, to very large: a multiscale study of the influence of fractures on physical properties of carbonate rocks" led by Fabio Trippetta. L. Chiaraluce is thanked for providing the dataset of the L'Aquila 2009 seismic sequence. We are grateful to Matt Ikari and the anonymous reviewer for the constructive reviews. All data are available via FTP transfer upon request to the corresponding author.

References

Agosta, F. (2008). Fluid flow properties of basin-bounding normal faults in platform carbonates, Fucino Basin, central Italy. *Geological Society London Special Publications*, *299*(1), 277–291. https://doi.org/10.1144/SP299.17

Agosta, F., & Kirschner, D. L. (2003). Fluid conduits in carbonate-hosted seismogenic normal faults of central Italy. *Journal of Geophysical Research*, *108*(B4), 2221. https://doi.org/10.1029/2002JB002013

Agosta, F., Prasad, M., & Aydin, A. (2007). Physical properties of carbonate fault rocks, fucino basin (Central Italy): Implications for fault seal in platform carbonates. *Geofluids*, *7*(1), 19–32. https://doi.org/10.1111/j.1468-8123.2006.00158.x

Al-Anzi, E., Al-Mutawa, M., Al-Habib, N., Al-Mumen, A., Nasr-El-Din, H. A., Alvarado, O., . . . Sandhu, D. (2003). Positive reactions in carbonate reservoir stimulation. *Oilfield Review*, *15*, 28–45.

Amato, A., Azzara, R., Basili, A. Chiarabba, C., Ciaccio, M. G., Cimini, G. B., . . . Selvaggi, G. (1998). Geodynamic evolution of the Northern Apennines from recent seismological studies. *Memorie Società Geologica Italiana*, *52*, 337–343.

Anderlini, L., Serpelloni, E., & Belardinelli, M. E. (2016). Creep and locking of a low-angle normal fault: Insights from the Altotiberina fault in the Northern Apennines (Italy). *Geophysical Research Letters*, *43*, 4321–4329. https://doi.org/10.1002/2016GL068604

Barchi, M. R., Minelli, G., & Pialli, G. (1998). The CROP 03 profile: A synthesis of results on deep structures of the northern Apennines. *Memorie Società Geologica Italiana*, *52*, 383–400.

Baud, P., Vinciguerra, S., David, C., Cavallo, A., Walker, E., & Reuschlé, T. (2009). Compaction and failure in high porosity carbonates: Mechanical data and microstructural observations. *Pure and Applied Geophysics*, *166*(5–7), 869–898. https://doi.org/10.1007/s00024-009-0493-2

Ben-Zion, Y., & Sammis, C. G. (2003). Characterization of Fault Zones. *Pure and Applied Geophysics*, *160*(3), 677–715. https://doi.org/10.1007/PL00012554

Billi, A., Salvini, F., & Storti, F. (2003). The damage zone-fault core transition in carbonate rocks: Implications for fault growth, structure and permeability. *Journal of Structural Geology*, *25*, 1779–1794. https://doi.org/10.1016/S0191-8141(03)00037-3

Birch, F. (1960). The velocity of compressional waves in rocks to 10 kilobars: 1. *Journal of Geophysical Research*, *65*(4), 1083–1102. https://doi.org/10.1029/JZ065i004p01083

Birch, F. (1961). The velocity of compressional waves in rocks to 10 kilobars: 2. *Journal of Geophysical Research*, *66*(7), 2199–2224. https://doi.org/10.1029/JZ066i007p02199

Boatwright, J., & Cocco, M. (1996). Frictional constraints on crustal faulting. *Journal of Geophysical Research*, *101*, 13895–13909. https://doi.org/10.1029/96JB00405

Boncio, P., & Lavecchia, G. (2000). A geological model for the Colfiorito earthquakes (September–October 1997, central Italy). *Journal of Seismology*, *4*(October), 345–356.

Burchfiel, B. C., Royden, L. H., van der Hilst, R. D., Hager, B. H., Chen, Z., King, R. W., . . . Kirby, E. (2008). A geological and geophysical context for the Wenchuan earthquake of 12 May 2008, Sichuan, People's Republic of China. *GSA Today*, *18*(7), 4. https://doi.org/10.1130/GSATG18A.1

Burke, M. M. (1987). *Compressional wave velocities in rocks from the Ivrea–Verbano and Strona–Ceneri zones, Southern Alps, Northern Italy: Implications for models of crustal structure*. Laramie: University of Wyoming.

Bussolotto, M., Benedicto, A., Moen-Maurel, L., & Invernizzi, C. (2015). Fault deformation mechanisms and fault rocks in micritic limestones: Examples from Corinth rift normal faults. *Journal of Structural Geology*, *77*, 191–212. https://doi.org/10.1016/j.jsg.2015.05.004

Caine, J. S. (1996). Fault zone arcitecture and permeability structure. *Geology*, *24*(11), 1025–1028.

Carpenter, B. M., Ikari, M. J., & Marone, C. (2016). Laboratory observations of time-dependent frictional strengthening and stress relaxation in natural and synthetic fault gouges. *Journal of Geophysical Research: Solid Earth*, *121*, 1183–1201. https://doi.org/10.1002/2015JB012136

Carpenter, B. M., Scuderi, M. M., Collettini, C., & Marone, C. (2014). Frictional heterogeneities on carbonate-bearing normal faults: Insights from the Monte Maggio Fault, Italy. *Journal of Geophysical Research: Solid Earth*, *119*, 9062–9076. https://doi.org/10.1002/2014JB011337

Chester, F. M., & Logan, J. M. (1986). Implications for mechanical properties of brittle faults from observations of the Punchbowl fault zone, California. *Pure and Applied Geophysics*, *124*(1–2), 79–106. https://doi.org/10.1007/BF00875720

Chiarabba, C., de Gori, P., & Boschi, E. (2009). Pore-pressure migration along a normal-fault system resolved by time-repeated seismic tomography. *Geology*, *37*(1), 67–70. https://doi.org/10.1130/G25220A.1

Chiaraluce, L. (2012). Unravelling the complexity of Apenninic extensional fault systems: A review of the 2009 L'Aquila earthquake (Central Apennines, Italy). *Journal of Structural Geology*, *42*, 2–18. https://doi.org/10.1016/j.jsg.2012.06.007

Chiaraluce, L., Barchi, M. R., Collettini, C., Mirabella, F., & Pucci, S. (2005). Connecting seismically active normal faults with Quaternary geological structures in a complex extensional environment: The Colfiorito 1997 case history (northern Apennines, Italy). *Tectonics*, *24*, TC1002. https://doi.org/10.1029/2004TC001627

Chiaraluce, L., Valoroso, L., Piccinini, D., Di Stefano, R., & De Gori, P. (2011). The anatomy of the 2009 L'Aquila normal fault system (central Italy) imaged by high resolution foreshock and aftershock locations. *Journal of Geophysical Research*, *116*, B12311. https://doi.org/10.1029/2011JB008352

Chiaraluce, L., Di Stefano, R., Tinti, E., Scognamiglio, L., Michele, M., Casarotti, E., . . . Marzorati, S. (2017). The 2016 Central Italy seismic sequence: A first look at the mainshocks, aftershocks, and source models. *Seismological Research Letters*, *88*, 1–15. https://doi.org/10.1785/0220160221

Collettini, C., Barchi, M. R., Chiaraluce, L., Mirabella, F., & Pucci, S. (2003). The Gubbio fault: Can different methods give pictures of the same object? *Journal of Geodynamics*, *36*(1–2), 51–66. https://doi.org/10.1016/S0264-3707(03)00038-3

Collettini, C., Carpenter, B. M., Viti, C., Cruciani, F., Mollo, S., Tesei, T., . . . Chiaraluce, L. (2014a). Fault structure and slip localization in carbonate-bearing normal faults: An example from the Northern Apennines of Italy. *Journal of Structural Geology*, *67*(PA), 154–166.

Collettini, C., De Paola, N., & Goulty, N. R. (2006). Switches in the minimum compressive stress direction induced by overpressure beneath a low-permeability fault zone. *Terra Nova*, *18*(3), 224–231. https://doi.org/10.1111/j.1365-3121.2006.00683.x

Collettini, C., Di Stefano, G., Carpenter, B., Scarlato, P., Tesei, T., Mollo, S., . . . Chiaraluce, L. (2014b). A novel and versatile apparatus for brittle rock deformation. *International Journal of Rock Mechanics and Mining Sciences*, *66*, 114–123. https://doi.org/10.1016/j.ijrmms.2013.12.005

Cowie, P. A., & Scholz, C. H. (1992). Growth of faults by accumulation of seismic slip. *Journal of Geophysical Research*, *97*, 11085–11095. https://doi.org/10.1029/92JB00586

Demurtas, M., Fondriest, M., Balsamo, F., Clemenzi, L., Storti, F., Bistacchi, A., & Di Toro, G. (2016). Structure of a normal seismogenic fault zone in carbonates: The Vado di Corno Fault, Campo Imperatore, Central Apennines (Italy). *Journal of Structural Geology*, *90*, 185–206. https://doi.org/10.1016/j.jsg.2016.08.004

De Paola, N., Collettini, C., Faulkner, D. R., & Trippetta, F. (2008). Fault zone architecture and deformation processes within evaporitic rocks in the upper crust. *Tectonics*, *27*, TC4017. https://doi.org/10.1029/2007TC002230

De Paola, N., Holdsworth, R. E., Viti, C., Collettini, C., & Bullock, R. (2015). Can grain size sensitive flow lubricate faults during the initial stages of earthquake propagation? *Earth and Planetary Science Letters*, *431*, 48–58. https://doi.org/10.1016/j.epsl.2015.09.002

Dieterich, J. H. (1979). Modeling of rock friction: 1. Experimental results and constitutive equations. *Journal of Geophysical Research*, *84*, 2161–2168. https://doi.org/10.1007/BF00876539

Doglioni, C., Mongelli, F., & Pialli, G. (1998). Boudinage of the alpine belt in the apenninic back-arc. *Memorie Società Geologica Italiana*, *52*, 457–468.

Dunham, R. J. (1962). Classification of carbonate rocks according to depositional texture. In *Classification of carbonate rocks—A symposium* (Vol. 38, pp. 108–121). Tulsa, OK: American Association of Petroleum Geologists.

Evans, J. P., Forster, C. B., & Goddard, J. V. (1997). Permeability of fault-related rocks, and implications for hydraulic structure of fault zones. *Journal of Structural Geology*, *19*(11), 1393–1404. https://doi.org/10.1016/S0191-8141(97)00057-6

Faulkner, D. R., Jackson, C. A. L., Lunn, R. J., Schlische, R. W., Shipton, Z. K., Wibberley, C. A. J., & Withjack, M. O. (2010). A review of recent developments concerning the structure, mechanics and fluid flow properties of fault zones. *Journal of Structural Geology*, *32*(11), 1557–1575. https://doi.org/10.1016/j.jsg.2010.06.009

Faulkner, D. R., Mitchell, T. M., Healy, D., & Heap, M. J. (2006). Slip on "weak" faults by the rotation of regional stress in the fracture damage zone. *Nature*, *444*(7121), 922–925. https://doi.org/10.1038/nature05353

Ferrill, D. A., Morris, A. P., McGinnis, R. N., Smart, K. J., & Ward, W. C. (2011). Fault zone deformation and displacement partitioning in mechanically layered carbonates: The Hidden Valley fault, central Texas. *American Association of Petroleum Geologists Bulletin*, *95*(8), 1383–1397. https://doi.org/10.1306/12031010065

Fondriest, M., Smith, S. A. F., Di Toro, G., Zampieri, D., & Mittempergher, S. (2012). Fault zone structure and seismic slip localization in dolostones, an example from the Southern Alps, Italy. *Journal of Structural Geology*, *45*, 52–67. https://doi.org/10.1016/j.jsg.2012.06.014

Fredrich, J. T., & Wong, T. (1986). Micromechanics of thermally induced cracking in three crustal rocks. *Journal of Geophysical Research*, *91*, 12743–12764. https://doi.org/10.1029/JB091iB12p12743

Frepoli, A., & Amato, A. (1997). Contemporaneous extension and compression in the Northern Apennines from earthquake fault-plane solutions. *Geophysical Journal International*, *129*(2), 368–388. https://doi.org/10.1111/j.1365-246X.1997.tb01589.x

Glover, P. W. J., Baud, P., Darot, M., Meredith, P. G., Boon, S. A., LeRavaleq, M., . . . Reusché, T. (1995). Alpha/beta phase transition in quartz monitored using acoustic emissions. *Geophysical Journal International*, *120*, 775–782.

Govoni, A., Marchetti, A., De Gori, P., Di Bona, M., Pio Lucente, F., Improt, L., . . . Piccinini, D. (2014). The 2012 Emilia seismic sequence (Northern Italy): Imaging the thrust fault system by accurate aftershock location. *Tectonophysics*, *622*, 44–55. https://doi.org/10.1016/j.tecto.2014.02.013

Gu, J. C., Rice, J. R., Ruina, A. L., & Tse, T. (1984). Slip motion and stability of a single degree of freedom elastic system with rate and state dependent friction. *Journal of the Mechanics and Physics of Solids*, *32*(3), 167–196.

Heap, M. J., Baud, P., Reuschlé, T., & Meredith, P. G. (2014a). Stylolites in limestones: Barriers to fluid flow? *Geology*, *42*(1), 51–54. https://doi.org/10.1130/G34900.1

Heap, M. J., Baud, P., Meredith, P. G., Vinciguerra, S., & Reuschlé, T. (2014b). The permeability and elastic moduli of tuff from Campi Flegrei, Italy: Implications for ground deformation modelling. *Solid Earth*, *5*(1), 25–44. https://doi.org/10.5194/se-5-25-2014

Heap, M. J., & Faulkner, D. R. (2008). Quantifying the evolution of static elastic properties as crystalline rock approaches failure. *International Journal of Rock Mechanics and Mining Sciences*, *45*(4), 564–573. https://doi.org/10.1016/j.ijrmms.2007.07.018

Hugman, R. H. H., & Friedman, M. (1979). Effects of texture and composition on mechanical behavior of experimentally deformed carbonate rocks. *American Association of Petroleum Geologists Bulletin*, *63*(9), 1478–1489. https://doi.org/10.1306/2F9185C7-16CE-11D7-8645000102C1865D

Ikari, M. J., Trütner, S., Carpenter, B. M., & Kopf, A. J. (2015). Shear behavior of DFDP-1 borehole samples from the Alpine Fault, New Zealand, under a wide range of experimental conditions. *International Journal of Earth Sciences*, *104*, 1523–1535. https://doi.org/10.1007/s00531-014-1115-5

Improta, L., Valoroso, L., Piccinini, D., & Chiarabba, C. (2015). A detailed analysis of wastewater-induced seismicity in the Val d'Agri oil field (Italy). *Geophysical Research Letters*, *42*, 2682–2690. https://doi.org/10.1002/2015GL063369

Kanamori, H., & Brodsky, E. E. (2004). The physics of earthquakes. *Reports on Progress in Physics*, *67*, 1429–1496. https://doi.org/10.1088/0034-4885/67/8/R03

Kanamori, H., & Anderson, D. L. (1975). Theoretical basis of some empirical relations in seismology. *Bulletin of the Seismological Society of America*, *65*, 1073–1095.

Latorre, D., Mirabella, F., Chiaraluce, L., Trippetta, F., & Lomax, A. (2016). Assessment of earthquake locations in 3-D deterministic velocity models: A case study from the Altotiberina Near Fault Observatory (Italy). *Journal of Geophysical Research: Solid Earth*, *121*, 8113–8135. https://doi.org/10.1002/2016JB013170

Lavecchia, G., Brozzetti, F., Barchi, M., Menichetti, M., & Keller, J. V. A. (1994). Seismotectonic zoning in east-central Italy deduced from an analysis of the Neogene to present deformations and related stress fields. *Geological Society of America Bulletin*, *106*(9), 1107–1120. https://doi.org/10.1130/0016-7606(1994)106<1107:SZIECI>2.3.CO;2

Leeman, J. R., Saffer, D. M., Scuderi, M. M., & Marone, C. (2016). Laboratory observations of slow earthquakes and the spectrum of tectonic fault slip modes. *Nature Communications*, *7*, 11104. https://doi.org/10.1038/ncomms11104

Marone, C. (1998). The effect of loading rate on static friction and the rate of fault healing during the earthquake cycle. *Nature*, *391*, 69–72. https://doi.org/10.1038/nature34157

Mavko, G., Mukerji, T., & Dvorkin, J. (2009). *The rock physics handbook: Tools for seismic analysis of porous media*. Cambridge, UK: Cambridge University Press.

McLaskey, G. C., & Yamashita, F. (2017). Slow and fast ruptures on a laboratory fault controlled by loading characteristics. *Journal of Geophysical Research: Solid Earth*, *122*, 3719–3738. https://doi.org/10.1002/2016JB013681

Micarelli, L., Benedicto, A., & Wibberley, C. A. J. (2006). Structural evolution and permeability of normal fault zones in highly porous carbonate rocks. *Journal of Structural Geology*, *28*(7), 1214–1227. https://doi.org/10.1016/j.jsg.2006.03.036

Michie, E. A. H. (2015). Influence of host lithofacies on fault rock variation in carbonate fault zones: A case study from the Island of Malta. *Journal of Structural Geology*, *76*, 61–79. https://doi.org/10.1016/j.jsg.2015.04.005

Michie, E. A. H., & Haines, T. J. (2016). Variability and heterogeneity of the petrophysical properties of extensional carbonate fault rocks, Malta. *Petroleum Geoscience*, *22*, 136–152. https://doi.org/10.1144/petgeo2015-027

Miller, S. A., Collettini, C., Chiaraluce, L., Cocco, M., Barchi, M. R., & Kaus, B. J. P. (2004). Aftershocks driven by a high-pressure CO_2 source at depth. *Nature*, *427*(6976), 724–727. https://doi.org/10.1038/nature02251

Mirabella, F., Barchi, M. R., Lupattelli, A., Stucchi, E., & Ciaccio, M. G. (2008). Insights on the seismogenic layer thickness from the upper crust structure of the Umbria-Marche Apennines (central Italy). *Tectonics*, *27*, TC1010. https://doi.org/10.1029/2007TC002134

Mitchell, T. M., & Faulkner, D. R. (2009). The nature and origin of off-fault damage surrounding strike-slip fault zones with a wide range of displacements: A field study from the Atacama fault system, northern Chile. *Journal of Structural Geology*, *31*(8), 802–816. https://doi.org/10.1016/j.jsg.2009.05.002

Mitchell, T. M., & Faulkner, D. R. (2012). Towards quantifying the matrix permeability of fault damage zones in low porosity rocks. *Earth and Planetary Science Letters*, *339–340*, 24–31. https://doi.org/10.1016/j.epsl.2012.05.014

Nissen, E., Jackson, J., Jahani, S., & Tatar, M. (2014). Zagros "phantom earthquakes" reassessed—The interplay of seismicity and deep salt flow in the Simply Folded Belt? *Journal of Geophysical Research: Solid Earth*, *119*, 3561–3583. https://doi.org/10.1002/2013JB010796

Rath, A., Exner, U., Tschegg, C., Grasemann, B., Laner, R., & Draganits, E. (2011). Diagenetic control of deformation mechanisms in deformation bands in a carbonate grainstone. *American Association of Petroleum Geologists Bulletin*, *95*(8), 1369–1381. https://doi.org/10.1306/01031110118

Riley, P. R., Goodwin, L. B., & Lewis, C. J. (2010). Controls on fault damage zone width, structure, and symmetry in the Bandelier Tuff, New Mexico. *Journal of Structural Geology*, *32*(6), 766–780. https://doi.org/10.1016/j.jsg.2010.05.005

Ruina, A. (1983). Slip instability and state variable friction laws. *Journal of Geophysical Research*, *88*, 10359–10370. https://doi.org/10.1029/JB088iB12p10359

Santantonio, M. (1994). Pelagic carbonate platforms in the geologic record: Their classification and sedimentary and paleotectonic evolution. *American Association of Petroleum Geologists Bulletin*, *78*(1), 122–141. https://doi.org/10.1306/BDFF9032-1718-11D7-8645000102C1865D

Savage, H. M., & Brodsky, E. E. (2011). Collateral damage: Evolution with displacement of fracture distribution and secondary fault strands in fault damage zones. *Journal of Geophysical Research*, *116*, B03405. https://doi.org/10.1029/2010JB007665

Scholz, C. H. (2002). *The mechanics of earthquakes and faulting*. Cambridge, UK: Cambridge University Press.

Scuderi, M. M., & Collettini, C. (2016). The role of fluid pressure in induced vs. triggered seismicity: Insights from rock deformation experiments on carbonates. *Scientific Reports*, *6*(1), 24852. https://doi.org/10.1038/srep24852

Scuderi, M. M., Marone, C., Tinti, E., Di Stefano, G., & Collettini, C. (2016). Precursory changes in seismic velocity for the spectrum of earthquake failure modes. *Nature Geoscience*, *9*(9), 695–700. https://doi.org/10.1038/ngeo2775

Shipton, Z. K., Soden, A., Kirkpatrick, J. D., Bright, A. M., & Lunn, R. J. (2006). How thick is a fault? Fault displacement thickness scaling revisited. In *Earthquakes: Radiated energy and the Physics of faulting* (pp. 193–198). Washington, DC: American Geophysical Union. https://doi.org/10.1029/170GM19

Smeraglia, L., Trippetta, F., Carminati, E., & Mollo, S. (2014). Tectonic control on the petrophysical properties of foredeep sandstone in the Central Apennines, Italy. *Journal of Geophysical Research: Solid Earth*, *119*, 9077–9094. https://doi.org/10.1002/2014JB011221

Smith, S. A. F., Di Toro, G., Kim, S., Ree, J. H., Nielsen, S., Billi, A., & Spiess, R. (2013). Coseismic recrystallization during shallow earthquake slip. *Geology*, *41*(1), 63–66. https://doi.org/10.1130/G33588.1

Stein, R. S., King, G. C., & Lin, J. (1992). Change in failure stress on the southern San Andreas fault system caused by the 1992 magnitude = 7.4 landers earthquake. *Science*, *258*(5086), 1328–1332. https://doi.org/10.1126/science.258.5086.1328

Tesei, T., Carpenter, B. M., Giorgetti, C., Scuderi, M. M., Sagy, A., Scarlato, P., & Collettini, C. (2017). Friction and scale-dependent deformation processes of large experimental carbonate faults. *Journal of Structural Geology*, *100*, 12–23. https://doi.org/10.1016/j.jsg.2017.05.008

Tesei, T., Collettini, C., Barchi, M. R., Carpenter, B. M., & Di Stefano, G. (2014). Heterogeneous strength and fault zone complexity of carbonate-bearing thrusts with possible implications for seismicity. *Earth and Planetary Science Letters*, *408*, 307–318. https://doi.org/10.1016/j.epsl.2014.10.021

Tinti, E., Scognamiglio, L., Michelini, A., & Cocco, M. (2016). Slip heterogeneity and directivity of the ML 6.0, 2016, Amatrice earthquake estimated with rapid finite-fault inversion. *Geophysical Research Letters*, *43*, 10745–10752. https://doi.org/10.1002/2016GL071263

Trippetta, F., Collettini, C., Barchi, M. R., Lupattelli, A., & Mirabella, F. (2013a). A multidisciplinary study of a natural example of a CO_2 geological reservoir in central Italy. *International Journal of Greenhouse Gas Control*, *12*, 72–83.

Trippetta, F., Collettini, C., Meredith, P. G., & Vinciguerra, S. (2013b). Evolution of the elastic moduli of seismogenic Triassic Evaporites subjected to cyclic stressing. *Tectonophysics*, *592*, 67–79.

Trippetta, F., Collettini, C., Vinciguerra, S., & Meredith, P. G. (2010). Laboratory measurements of the physical properties of Triassic Evaporites from Central Italy and correlation with geophysical data. *Tectonophysics*, *492*(1–4), 141–149.

Valoroso, L., Chiaraluce, L., & Collettini, C. (2014). Earthquakes and fault zone structure. *Geology*, *42*(4), 343–346. https://doi.org/10.1130/G35071.1

Verberne, B. A., He, C., & Spiers, C. J. (2010). Frictional properties of sedimentary rocks and natural fault gouge from the Longmen Shan fault zone, Sichuan, China. *Bulletin of the Seismological Society of America*, *100*(5B), 2767–2790. https://doi.org/10.1785/0120090287

Verberne, B. A., Plumper, O., Matthijs de Winter, D. A., & Spiers, C. J. (2014). Superplastic nanofibrous slip zones control seismogenic fault friction. *Science*, *346*(6215), 1342–1344. https://doi.org/10.1126/science.1259003

Verberne, B. A., Niemeijer, A. R., De Bresser, J. H. P., & Spiers, C. J. (2015). Mechanical behavior and microstructure of simulated calcite fault gouge sheared at 20–600??C: Implications for natural faults in limestones. *Journal of Geophysical Research: Solid Earth*, *120*, 8169–8196. https://doi.org/10.1002/2015JB012292

Vinciguerra, S., Trovato, C., Meredith, P. G., Benson, P. M., Troise, C., & Natale, G. D. (2006). Understanding the seismic velocity structure of Campi Flegrei caldera (Italy): From the laboratory to the field scale. *Pure and Applied Geophysics*, *163*(10), 2205–2221. https://doi.org/10.1007/s00024-006-0118-y

Violay, M., Nielsen, S., Spagnuolo, E., Cinti, D., Di Toro, G., & Di Stefano, G. (2013). Pore fluid in experimental calcite-bearing faults: Abrupt weakening and geochemical signature of co-seismic processes. *Earth and Planetary Science Letters*, *361*, 74–84. https://doi.org/10.1016/j.epsl.2012.11.021